


Predicting maximum force in SPIF for different materials

Rafael Gustavo Schreiber¹ , Lucas Santos Savi Mondo¹,
Andrison Rodrigues Teixeira², Anderson Daleffe³, Lirio Schaeffer²

¹Instituto Federal de Educação, Ciência e Tecnologia de Santa Catarina. R.Heitor Villa Lobos, 225, 88506-400, Lages, SC, Brasil.

²Universidade Federal do Rio Grande do Sul. Avenida Bento Gonçalves, 9500, Agronomia, 90010-150, Porto Alegre, RS, Brasil.

³Centro Universitário UNISATC. Rua Pascoal Meller, 73, Bairro Universitário, 88805-380, Criciúma, SC, Brasil.

e-mail: rafael.schreiber@ifsc.edu.br, lucas.savimondo@gmail.com, andrison@g1equipamentos.com.br, anderson.daleffe@satc.edu.br, schaefer@ufrgs.br

ABSTRACT

Knowing the importance of predicting acting forces during the formation process, our research has conducted 27 Single Point Incremental Forming (SPIF) experiments in hyperboloid format, followed by Finite Element Method (FEM) simulations and regression equations were determined to estimate the maximum axial force in the process. ANOVA analysis of variance was used to determine the significance of material parameters in the maximum axial force response. A multiple linear regression model was constructed to estimate the maximum axial force in the SPIF process. After the experiments, we were able to identify that the maximum axial force increases according to an increase in tool radius, sheet initial thickness, and strength coefficient values, as well as according to the decrease in the strain-hardening exponent. The FEM simulations are in agreement with the experimental values found, and the linear regression model has proven to be efficient to describe results, with R² of 98.85% and a maximum percentage error of 11.5%.

Keywords: SPIF; Maximum Axial Force; FEM; Multiple Regression.

1. INTRODUCTION

In Single Point Incremental Forming (SPIF), the final shape of the piece being manufactured is defined by the hemispheric-tipped tool's trajectory, which progressively deforms a plane sheet [1]. This is a flexible process that does not require dedicated tools [2] and can be used in the fabrication of individual parts or small lots of parts [3, 4].

Compared to conventional sheet formation processes, in SPIF the necessary conformation force is reduced due to localized and successive deformations that occur during the process [5]. Nevertheless, it is fundamental to be able to predict the acting forces during the process to select the equipment that will be used, such as a CNC milling machine [6–8], a CNC lathe [9–11], a robotic arm [12–14], or a machine designed for this purpose [15, 16].

The process parameters influence the SPIF acting forces, and as such, with an increase in tool radius [17], initial sheet thickness, or step-down [18], there is also an increase in the force required to achieve the deformation. Materials with greater yield strength [18, 19] also require greater force for the deformation to occur. However, as tool rotation increases [20], and with it the process temperature [21], there is a decrease in the required force. The feed rate on the other hand presents little influence over the forces applied to the ISF process [22].

DUFLOU *et al.* [23] carried out a study with Al 3003-O and Al 3103-O, in which they found that about tool radius, the sheet's thickness, and the wall angle, the step-down is the least relevant factor among the acting forces in the ISF process. Therefore, the authors suggest that the step-down parameter can be increased, allowing for greater process productivity without a significant impact on the acting forces. The authors elaborated force regression equations as a function of each analyzed parameter.

In the SPIF process, the axial force component is the one that presents greater intensity when compared to radial and tangential components [24, 25]. Depending on the shape of the piece that is being conformed by the

SPIF, the force versus time graph presents different characteristics [26]. However, in the most common shapes (truncated cone and hyperboloid), it is possible to observe that the axial force component shows a peak during the tool's axial movement against the sheet, followed by a lower level during the tool's circular interlocking [19, 27].

LI *et al.* [28] have developed an analytical model based on the superior limit approach to predict tangential forces in SPIF for aluminum 7075-O, applying truncated cone conformation with different wall angles and step-downs. This model showed greater accuracy for step-down values lower than 0.5 mm.

DUFLOU *et al.* [27] developed regression equations to estimate the peak axial force, mean axial force and tangential force in SPIF applied to Al 3003-O sheets. The influence parameters chosen to estimate the forces in the process were step-down, wall angle, tool diameter, and initial sheet thickness.

In studies by AERENS *et al.* [19], regression equations were also developed to estimate peak axial force, mean axial force, radial force, and tangential force. However, in this work equations were defined for different materials: DC01, AISI 304, AA5754, and AA3003. The influence variables selected in the regression equations of this research were step-down, wall angle, tool diameter, initial sheet thickness, and tensile strength.

BANSAL *et al.* [29] and CHANG *et al.* [5] have also developed analytical models to predict ISF force based on stress and the contact area between the piece and the tool. Their models presented greater accuracy when compared to the ones proposed by AERENS *et al.* [19].

The Finite Element Method (FEM) can be used to predict the behavior of materials under different conditions, such as contact stresses [30] and working conditions [31] in bearings; or residual stresses [32] and thermo-mechanical behavior [33] of welded joints. Furthermore, the combination of FEM and multiple regression models have been used to predict the mechanical properties of different materials [34, 35], or to predict process parameters [36].

Despite there being several models that allow an estimation of ISF's mean forces, there is still the need to estimate maximum force, which has a fundamental role in the selection of appropriate equipment to perform the forming process. Therefore, our work aims to evaluate the influence of material properties, sheet thickness, and tool diameter on the axial force applied to the SPIF process. For this, 27 experiments were carried out. The axial force was measured using extensometers installed in each tool. Analysis of variance was performed to verify the significance of the parameters used in the axial force response. Then, FEM and multiple regression were used to estimate the maximum axial force in the process.

2. MATERIALS AND METHODS

In this study, 27 SPIF experiments were conducted to test the fabrication of hyperboloids with different materials, sheet thicknesses, and tool radii to evaluate what influence these parameters exert on the maximum axial force Fz_{max} . To validate the force results found in the experiments, three FEM simulations were made. In addition, an analysis of variance and multiple regressions were also conducted to introduce a prediction method for maximum axial force for each process condition. In Table 1, we have indicated the symbology and the measuring units of the parameters used during the course of this work.

To describe the plastic behavior of each material, Hollomon's equation (Equation 1) was used, where σ is the equivalent stress, C is the strength coefficient, φ is the equivalent strain and n is the strain-hardening exponent.

$$\sigma = C\varphi^n \quad (1)$$

For the experiments, the materials used were AA1200-H14 aluminum, SAE1008 steel, and C268 brass sheets, with mechanical thicknesses and properties as indicated in Table 2. The mechanical properties of the materials presented in Table 2 were based on studies by SCHREIBER *et al.* [37] for AA1200-H14, HAAG and FERRANTI [38] for SAE1008, and MAXIMILIANO *et al.* [39] for C268.

The three materials were selected based on previous research in the area of sheet metal forming [30–32]. Three commercial thicknesses were selected for each material. However, in the case of SAE1008 steel, the limit of 0.9 mm in thickness was established, as the machine used could not deform sheets of this material with greater thickness, due to a force limitation.

2.1. SPIF experiments with force measurement

For this research, the pieces were formed in a hyperboloid shape (Figure 1a) using the SPIF process. The hyperboloid shape allows variation in the piece's wall angle (between θ_0 and θ) and thickness (between s_0 and s) according to h depth. All experiments were conducted until the pieces reached the maximum wall angle and

Table 1: Parameters.

| SYMBOL | PARAMETER | UNIT |
|-------------------|--------------------------------|------|
| C | Strength coefficient | MPa |
| d | Final dimension | mm |
| d ₀ | Initial diameter | mm |
| Fz | Axial force | N |
| Fz _{max} | Maximum axial force | N |
| h | Maximum deep | mm |
| MAE | Mean Absolute Error | – |
| N | Number of test sample elements | – |
| n | Strain-hardening Exponent | – |
| PE | Percentage Error | % |
| PE _{max} | Maximum Percentage Error | % |
| RMSE | Root Mean Squared Error | – |
| Rm | Tensile Strength | MPa |
| R _t | Tool radius | mm |
| s | Final thickness | mm |
| s ₀ | Initial thickness | mm |
| y _{exp} | Experimental value | – |
| y _p | Predicted value | – |
| φ | Equivalent strain | – |
| φ ₁ | Major strain | – |
| φ ₂ | Minor strain | – |
| φ ₃ | Thickness strain | – |
| σ | Equivalent stress | – |
| θ | Final wall angle | rad |
| θ ₀ | Initial wall angle | rad |

Table 2: Material Properties.

| MATERIAL | INITIAL THICKNESS, S ₀ (mm) | YIELD STRENGTH (MPa) | TENSILE STRENGTH, Rm (MPa) | ELONGATION (%) | MODULUS OF ELASTICITY (GPa) | STRENGTH COEFFICIENT, C (MPa) | STRAIN-HARDENING EXPONENT, n (–) |
|------------|--|----------------------|----------------------------|----------------|-----------------------------|-------------------------------|----------------------------------|
| AA1200-H14 | 0.50 / 0.80 / 1.20 | 97 | 117 | 3.6 | 70 | 181.45 | 0.1080 |
| SAE1008 | 0.60 / 0.75 / 0.90 | 265 | 359 | 41.5 | 190 | 619.86 | 0.2163 |
| C268 | 0.50 / 0.81 / 1.06 | 296 | 413 | 37.5 | 105 | 734.28 | 0.2624 |

presented a crack, at this moment, the depth displayed on the CNC machine panel was registered. Figure 1b shows a hyperboloid conformation in the final experiment, indicating the location of the crack and the support pieces used to fixate the sheet, constituted of a rig, backing plate, and blank-holder.

Unidirectional strain gauges, brand Excel, and model PA-06-060BA-350L were installed in the conformation tool to measure the axial force during the process since this is the most intense force in the SPIF process [19]. Figure 2 presents how the link between the strain gauges (Wheatstone bridge circuit), in which four strain gauges (R₁ to R₄), are presented and where bridge exciting voltage is indicated with a Vs, and bridge

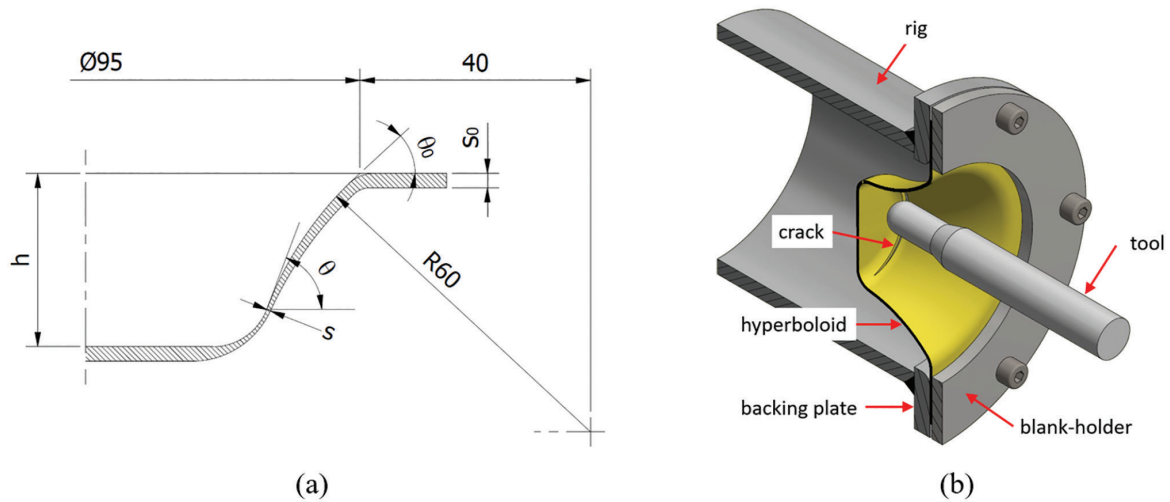


Figure 1: Hyperboloid shape used in the experiments (a) and Experiments' configuration (b).

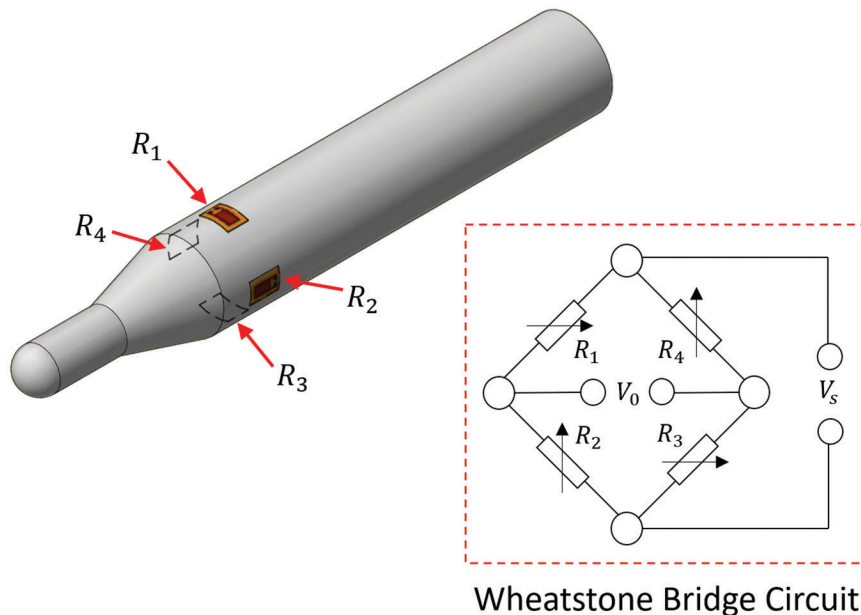


Figure 2: Wheatstone bridge circuit in the tool.

exit voltage with a V_0 . Data acquisition was made using a microcontroller board Arduino MEGA 2560 R3 connected to a computer.

Experiments were made in a Nardini LOGIC 195VS CNC lathe. Figure 3a presents the configuration used for the CNC lathe experiments, indicating the tool, the sheet (fixated on a support system), as well as a turret, chuck, and the z-axis force measuring system constituted of strain gauges and microcontroller board.

Figure 3b indicates the tool trajectory and of the part in the CNC lathe, considering that the tool's linear trajectories were conducted by the turret (with a feed rate of 100 mm/min), and the circular trajectories were made by the sheet fixed on the chuck (with a rotation speed of 2 rpm). In the experiments, we used a 1 mm step-down, and lubrication was added with a thin layer of VG100 oil. The tool used in this study were fabricated in SAE 1045 steel, quenched, and tempered, with radii of 3, 5, and 7.5 mm.

Before each experiment, the sheets were etched by electrochemical process from a grid of circles of initial diameter $d_0 = 1$ mm. After forming, each circle turned into an ellipse deformed only in one direction with final dimension d (Figure 4).

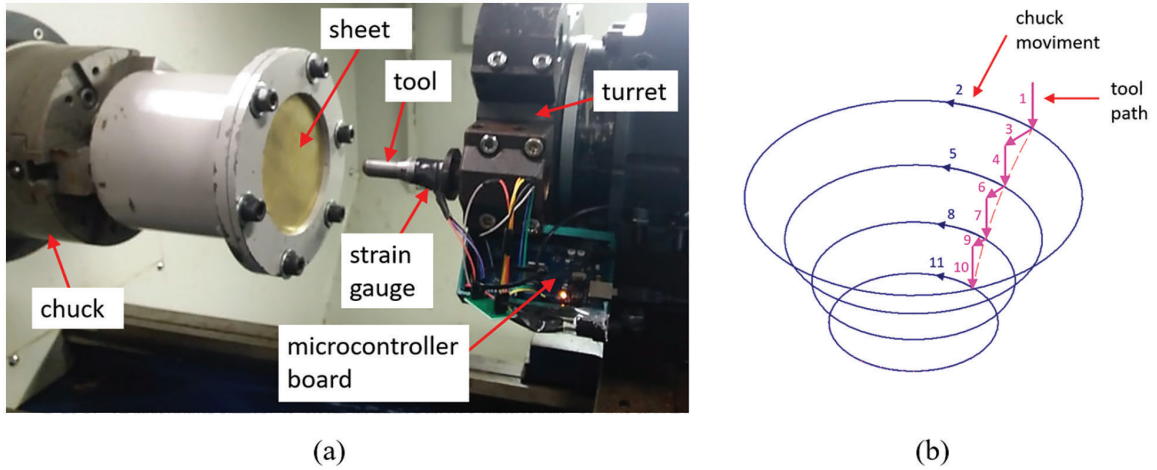


Figure 3: Experiment configuration in a CNC lathe (a) and Tool trajectory in the experiments (b).

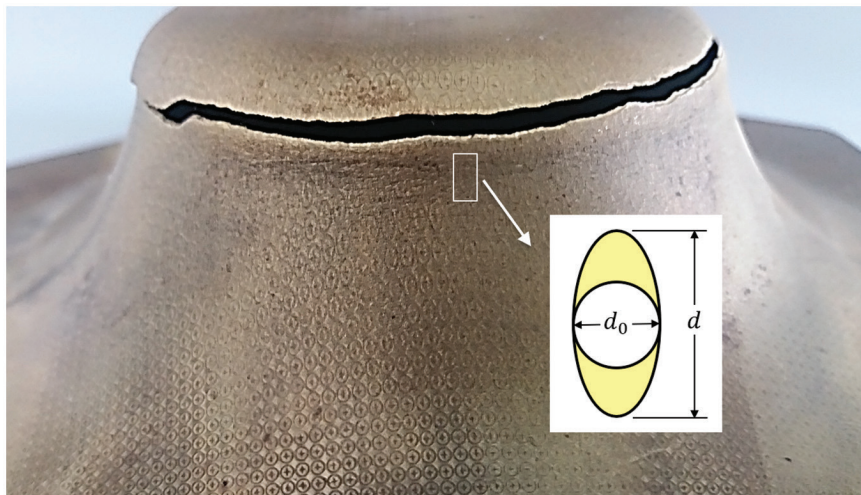


Figure 4: Circle grid after sheet metal strain.

The major strain (φ_1) was calculated using Equation 2. In the case of the hyperboloid shape the minor strain $\varphi_2 = 0$, while the thickness strain (φ_3) is defined as $\varphi_3 = -\varphi_1$, assuming a constant volume. The final thickness (s) was estimated according to Equation 3, where s_0 is the initial thickness.

$$\varphi_1 = \ln\left(\frac{d}{d_0}\right) \tag{2}$$

$$s = s_0 e^{\varphi_3} \tag{3}$$

2.2. Statistical analysis

To evaluate the effects of material parameters, tool radius, and initial sheet thickness on the maximum axial force response, an ANOVA analysis of variance was conducted. To determine whether the data obtained were parametric, the Shapiro-Wilk test and the Levene test were performed, to assess variance normality and homogeneity, respectively. Statistical analysis was performed using RStudio software, and $p < 0.05$ was used as a criterion for statistical significance in the analysis.

After defining the parameters of statistical significance using ANOVA, multiple linear regression was used to predict Fz_{max} , using the RStudio software. Then, four linear regression models were created to estimate the maximum axial force. These four regression models were based on R_t (tool radius), s_0 (initial thickness), and

different material properties: the first model was created as a function of C (strength coefficient); the second as a function of n (strain-hardening exponent); the third as a function of C and n ; the fourth as a function of R_m (tensile strength).

To evaluate the accuracy of each model, that is, to evaluate the prediction error rates as well as model performance in each regression analysis, the metrics R^2 (Coefficient of Determination), MAE (Mean Absolute Error), and RMSE (Root Mean Squared Error) were used. Equations 4 and 5 were used to calculate MAE and RMSE values, where N is the number of test sample elements, y_{exp} is the experimental value and y_p is the predicted value by the regression model.

$$MAE = \frac{1}{N} \sum_{i=1}^N |y_{exp} - y_p| \quad (4)$$

$$RMSE = \sqrt{\frac{1}{N} \sum_{i=1}^N (y_{exp} - y_p)^2} \quad (5)$$

AIC (Akaike Information Criterion) and BIC (Bayesian Information Criterion) were used to complement the analysis and select the model that best fits the data. Additionally, an analysis of variance was performed between the nested models, that is, between models 1 and 2, as well as between models 1 and 3. The lowest value of RSS (Residual Sum of Squares) was used as a reference to select the model best describes the maximum force in experiments. Model 4 was excluded from this last analysis as it is not derived from the others.

A general equation was determined to estimate the maximum axial force in a SPIF process, using multiple linear regression, according to the model that best fits the data. To validate the regression models obtained in this work, we used Equation 6, where PE is the percentage error, y_p is the data predicted by the regression model and y_{exp} is the data obtained in the experiments.

$$PE = \frac{|y_{exp} - y_p|}{y_{exp}} 100 \quad (6)$$

2.3. FEM simulations

Aiming to validate the axial force data obtained in the experiments using strain gauges, three simulations were made using the Finite Elements Method (FEM) with the Simufact Forming software. The experiments selected for comparison with the simulation were numbers 7, 14, and 25 (Table 3), to compare axial force values in different materials and validate the measurements. The results obtained in the simulations were compared to the experimental data, and the maximum axial force percentage error was calculated for each simulation using Equation 6. MAE (Eq. 4) and RMSE (Eq. 5) were also calculated to assess the prediction accuracy of the finite element model. In this case, y_p was considered the predicted value by the finite element model.

Simulations were made with Simufact Forming software, which uses the implicit method. A 3D simulation type with solid-shell type elements was used within the Sheet Metal Forming module in the software. The mesh created for each sheet was configured using the mesher “Sheetmesh” and the type of element used “solid-shell”. The mesh size was set at 1 mm edge length, with 3 layers under the thickness. In this configuration, each solid shell has a hexahedral shape. Also, shells are layers of integration points within each element under the thickness. In each simulation, the blank was subdivided into 6716 elements.

For mesh quality analysis, a simplified remeshing method was used, based on the strain change criterion. In each sub-model, remeshing occurred after the main strain reached a value above 0.4. Therefore, only one remeshing was performed in each sub-model, to obtain less processing time in the simulation.

Figure 5 presents the assembly of the simulation, constituted of a tool, sheet, backing plate, and blank-holder. To reduce the simulation’s total time, the initial hyperboloid diameter was decreased from 95 mm to 65 mm, and all other dimensions were kept the same as the ones used in the experiments.

In the definition of degrees of freedom (DoF), the interactions between each body in the simulation were defined. In the interaction between sheet and blank-holder, as well as for sheet and backing plate, the “glued” contact was established, In the “glued” configuration, relative movement between two bodies in contact is not possible. In the relationship between tool and sheet, the “touching” interaction was defined, as when the bodies

Table 3: SPIF conformability experimental results.

| EXP. | MATERIAL | C (MPa) | n (-) | R_t (mm) | s0 (mm) | h (mm) | ϕ_1 (-) | s (mm) | Fz_{max} (N) |
|------|------------|---------|--------|------------|---------|--------|--------------|--------|----------------|
| 1 | AA1200-H14 | 181.45 | 0.1080 | 3.0 | 0.50 | 30 | 1.192 | 0.182 | 323.4 |
| 2 | AA1200-H14 | 181.45 | 0.1080 | 3.0 | 0.80 | 37 | 1.331 | 0.198 | 515.0 |
| 3 | AA1200-H14 | 181.45 | 0.1080 | 3.0 | 1.20 | 40 | 1.414 | 0.219 | 939.6 |
| 4 | AA1200-H14 | 181.45 | 0.1080 | 5.0 | 0.50 | 26 | 1.264 | 0.170 | 471.5 |
| 5 | AA1200-H14 | 181.45 | 0.1080 | 5.0 | 0.80 | 36 | 1.309 | 0.203 | 745.1 |
| 6 | AA1200-H14 | 181.45 | 0.1080 | 5.0 | 1.20 | 39 | 1.331 | 0.238 | 1205.3 |
| 7 | AA1200-H14 | 181.45 | 0.1080 | 7.5 | 0.50 | 29 | 1.192 | 0.182 | 638.9 |
| 8 | AA1200-H14 | 181.45 | 0.1080 | 7.5 | 0.80 | 36 | 1.240 | 0.217 | 918.6 |
| 9 | AA1200-H14 | 181.45 | 0.1080 | 7.5 | 1.20 | 41 | 1.240 | 0.260 | 1595.0 |
| 10 | SAE1008 | 619.86 | 0.2163 | 3.0 | 0.60 | 32 | 1.141 | 0.160 | 1485.9 |
| 11 | SAE1008 | 619.86 | 0.2163 | 3.0 | 0.75 | 36 | 1.491 | 0.180 | 2157.0 |
| 12 | SAE1008 | 619.86 | 0.2163 | 3.0 | 0.90 | 37 | 1.674 | 0.225 | 2508.8 |
| 13 | SAE1008 | 619.86 | 0.2163 | 5.0 | 0.60 | 34 | 1.141 | 0.160 | 2000.7 |
| 14 | SAE1008 | 619.86 | 0.2163 | 5.0 | 0.75 | 37 | 1.352 | 0.207 | 2668.5 |
| 15 | SAE1008 | 619.86 | 0.2163 | 5.0 | 0.90 | 37 | 1.434 | 0.286 | 3203.7 |
| 16 | SAE1008 | 619.86 | 0.2163 | 7.5 | 0.60 | 34 | 1.141 | 0.160 | 2947.9 |
| 17 | SAE1008 | 619.86 | 0.2163 | 7.5 | 0.75 | 37 | 1.373 | 0.203 | 3567.3 |
| 18 | SAE1008 | 619.86 | 0.2163 | 7.5 | 0.90 | 37 | 1.562 | 0.252 | 4508.8 |
| 19 | C268 | 734.28 | 0.2618 | 3.0 | 0.50 | 22 | 0.764 | 0.233 | 1071.1 |
| 20 | C268 | 734.28 | 0.2618 | 3.0 | 0.81 | 27 | 0.970 | 0.307 | 2067.6 |
| 21 | C268 | 734.28 | 0.2618 | 3.0 | 1.06 | 28 | 1.059 | 0.368 | 3378.4 |
| 22 | C268 | 734.28 | 0.2618 | 5.0 | 0.50 | 22 | 0.938 | 0.196 | 1450.2 |
| 23 | C268 | 734.28 | 0.2618 | 5.0 | 0.81 | 27 | 1.114 | 0.266 | 2619.8 |
| 24 | C268 | 734.28 | 0.2618 | 5.0 | 1.06 | 29 | 1.141 | 0.339 | 3566.6 |
| 25 | C268 | 734.28 | 0.2618 | 7.5 | 0.50 | 21 | 0.906 | 0.202 | 2110.8 |
| 26 | C268 | 734.28 | 0.2618 | 7.5 | 0.81 | 27 | 1.030 | 0.289 | 3672.7 |
| 27 | C268 | 734.28 | 0.2618 | 7.5 | 1.06 | 29 | 1.087 | 0.357 | 5413.8 |

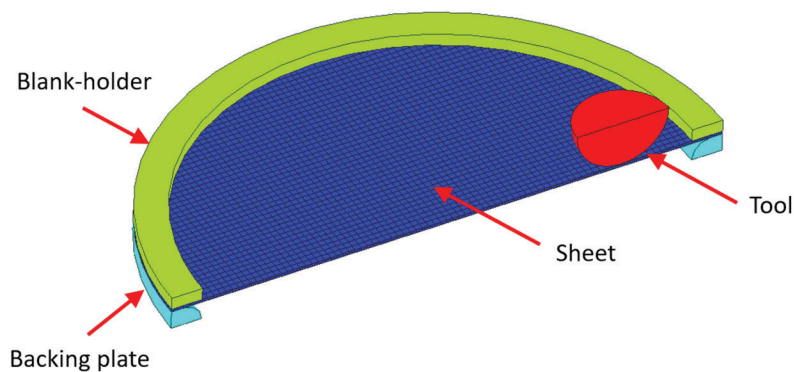


Figure 5: Assembly of SPIF test to FEM.

can slide over each other. The friction coefficient selected was 0.1 (Coulomb Law). No contact algorithm was considered.

For the tool, the blank-holder, and the backing plate, the configuration of “rigid die without heat conduction” was defined. The ambient temperature was considered 20°C.

The movements during each simulation were defined using “tabular motion”, in which a table is established containing all the coordinates for which the displacement of a body will occur. This option allows the rotation and translation of bodies. Instead of interspersing the process movements between chuck movement and tool movement, as performed in the experiments (Figure 5), it was configured that all movements that produce strain in the sheet would be performed only by the tool. In this way it was possible to obtain only one motion table, simplifying the construction of the model.

The tabular motion built for the movements was defined for each tool displacement point. For circular tool displacements (equivalent to chuck movement), each circle was divided into 90 points. The time elapsed between each point was calculated as a function of the linear feed speed of the tool (100 mm/min) and the chuck rotation (2 rpm). This motion table was built using Microsoft Excel and later imported by Simufact Forming.

In each simulation sub-model, the plasticity model considered was the Hollomon model for cold forming (Equation 1). The materials used were considered isotropic in the simulation.

3. RESULTS AND DISCUSSION

3.1. Experimental results

We have listed in Table 3 the maximum axial force values for each SPIF experiment according to material, tool radius, and initial thickness. The maximum axial force was obtained for the highest peak point in the force versus time graph for each experiment. The C and n parameters listed in Table 3 refer to Hollomon’s equation. Table 3 also presents the major strain results as well as the final thickness results in each experiment.

In Figure 6 we present a graph for axial force versus time considering SAE1008 steel with $s_0 = 0.75$ mm and using different tool radii ($R_t = 7.5, 5,$ and 3 mm). In this figure, we were able to verify the force peak points in places where the tool moved on the z-axis, followed by a lower force level due to circular trajectories.

For the experiment with $R_t = 7.5$ mm, we have indicated the point of maximum axial force ($F_{z_{max}}$), considering that after that point the force gradually reduces until an abrupt reduction in force occurs (also indicated in Figure 6. The abrupt reduction point in axial force indicates that a crack was initiated during the experiment. Figure 6 indicates that the bigger the tool radius the greater the axial force required by the machine. This tendency is accorded with other studies [5, 19, 29, 33] and can be explained as a consequence of contact area [17, 29].

Figure 7 presents a comparison between the axial force graphs for different initial thicknesses ($s_0 = 0.90, 0.75,$ and 0.60 mm) for SAE1008 steel, using an $R_t = 5$ mm tool radius. In this figure, we can see that the bigger that sheet’s thickness, the greater the axial force required by the machine to perform the forming process, as was reported in other studies [5, 19, 23, 29]. This tendency is related to the fact that with an increase in thickness, more material will have to be deformed by the tool, requiring more force [40].

In Figure 8 we present a comparison of the axial force required according to material: C268 with $s_0 = 0.81$ mm, SAE1008 with $s_0 = 0.75$ mm and AA1200-H14 with $s_0 = 0.80$ mm, in which all experiments used tool radius $R_t = 5$ mm. It is possible to note in this Figure that the materials with greater tensile strength (Table 2) require greater force to be deformed, as was verified in the studies by AERENS *et al.* [19].

The force graphs presented in Figures 6, 7, and 8 present a similar tendency to the one presented in other studies using the hyperboloid shape [27, 35, 36], and as such it is possible to observe that the axial force increases until it reaches a peak point, followed by a decrease in axial force intensity until a crack occurs in the sheet.

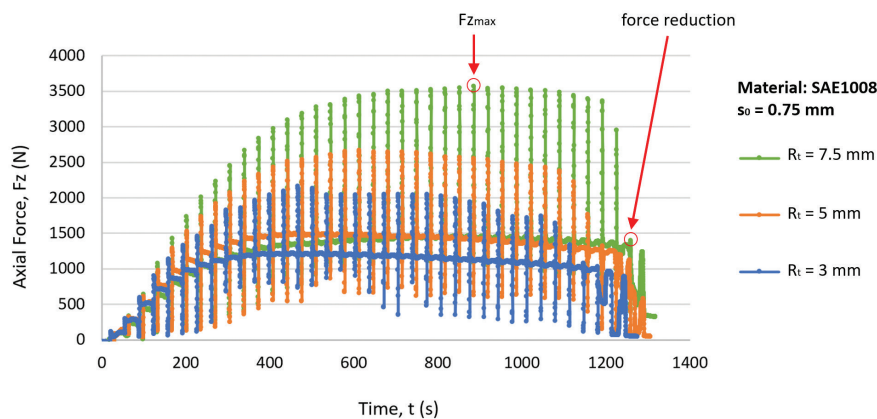


Figure 6: Graph comparing forces between different tool radii for SAE1008 and $s_0 = 0.75$ mm.

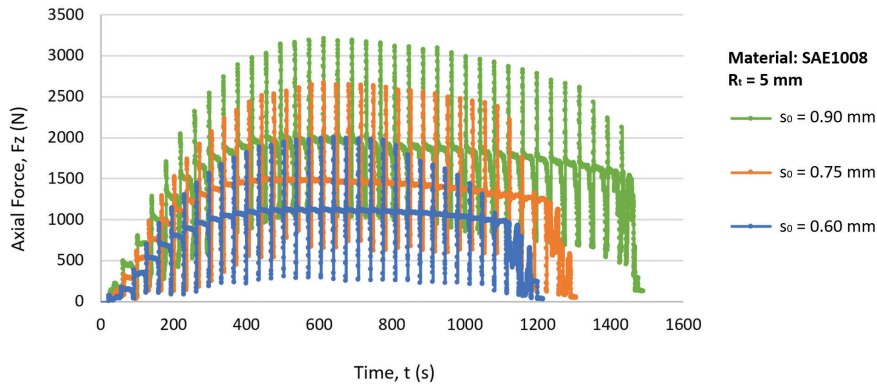


Figure 7: Graph comparing forces between different thicknesses for SAE1008 and $R_t = 5$ mm.

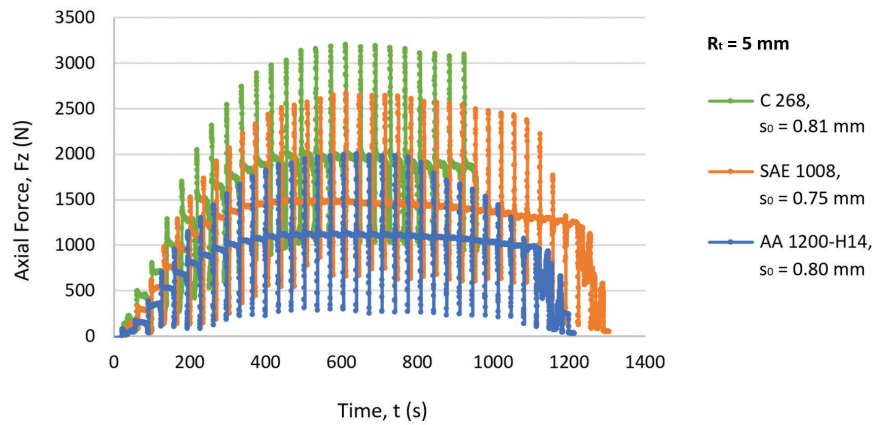


Figure 8: Graph comparing forces between different materials with $R_t = 5$ mm.

3.2. Statistical analysis results

Three-way ANOVA (Material + $R_t + s_0$) model was created, which has shown a significant effect on the material [$F(3, 21) = 41.43; p < 0.001$], on the tool radius [$F(1, 21) = 29.57; p < 0.001$], and on the initial sheet thickness [$F(1, 21) = 24.82; p < 0.001$] at the maximum axial force response. This result confirms the results obtained in other studies [16, 17, 19] also require greater force for the deformation to occur. In this analysis, both the Shapiro-Wilk test and the Levene test indicated normalcy in the residue and homogeneity in the variances.

After that, four multiple linear regression models were created to estimate the maximum axial force. Each regression model was created based on different parameters, as indicated in Table 4.

As indicated in Table 4, despite model 3 showing multicollinearity between the parameters C and n (which are intrinsic properties of the materials), this model was more accurate and fitted the data better than the others. This conclusion can be made because, when compared with the others, model 3 showed a higher R^2 value (98.85%), as well as lower MAE and RMSE values. When comparing the models through the AIC and BIC criteria, model 3 was also shown to fit better with the data.

When performing an analysis of variance between models 1 and 2, as well as between models 1 and 3. For both comparisons, a result of $p < 0.001$ was obtained, which means that these models are statistically different. Furthermore, in both comparisons, the value of RSS (Residual Sum of Squares) is lower for model 3, indicating that this model better describes the maximum force in the experiments.

Table 4: Comparison between regression models.

| MODEL NAME | PARAMETERS | R^2 | MAE | RMSE | AIC | BIC |
|------------|------------------|--------|-------|-------|-------|-------|
| model 1 | R_t, s_0, C | 95.10% | 228.3 | 228.4 | 400.5 | 412.2 |
| model 2 | R_t, s_0, n | 91.99% | 308.0 | 368.6 | 413.7 | 425.4 |
| model 3 | R_t, s_0, C, n | 98.85% | 96.6 | 139.8 | 369.4 | 386.3 |
| model 4 | R_t, s_0, R_m | 95.78% | 207.3 | 267.7 | 396.5 | 408.1 |

After these comparisons, we were able to obtain Equation 7, based on model 3. This equation relates the maximum axial force according to tool radius, initial sheet thickness, strength coefficient, material strain-hardening exponent, and the interaction between these parameters. The maximum percentage error obtained by Equation 7 in the experiments was 11.5%, as indicated between square brackets beside the equation.

$$\begin{aligned}
 Fz_{max} = & 416.7 + 172.8R_t + 275s_0 + 0.1479C - 5555n + 225.5R_t s_0 \\
 & + 0.8436R_t C + 5.189s_0 C - 2929R_t n - 6284s_0 n + 1.585R_t s_0 C \\
 & - 3727R_t s_0 n [PE_{max} = 11.5\%]
 \end{aligned}
 \tag{7}$$

In the multiple linear regression of model 3, interactions between parameters that were not presented in Equation 7 are not statistically significant. Furthermore, as indicated in Equation 7, the increase in tool radius, initial thickness, and strength coefficient increased maximum axial force. However, the strain-hardening exponent had an inverse effect, since with its increase there is a decrease in maximum force. The same effect can be observed in every interaction with the strain-hardening exponent, which presents negative sign constants.

Unlike the AERENS *et al.* [19]’s model, which used tensile strength in the force equation, in this work we have used the strength coefficient and the strain-hardening exponents in Hollomon’s equation because they allowed for the creation of a regression equation that better described the experimental results. Furthermore, Equation 7 has also not taken into consideration the step-down, since, according to DUFLOU *et al.* [23], that is the parameter that least influences the force.

Figure 9 indicates response surface plots for the multiple linear regression, according to model 3, for each material. In these graphs, it is possible to observe that the tendency to increase the maximum axial force (Fz_{max})

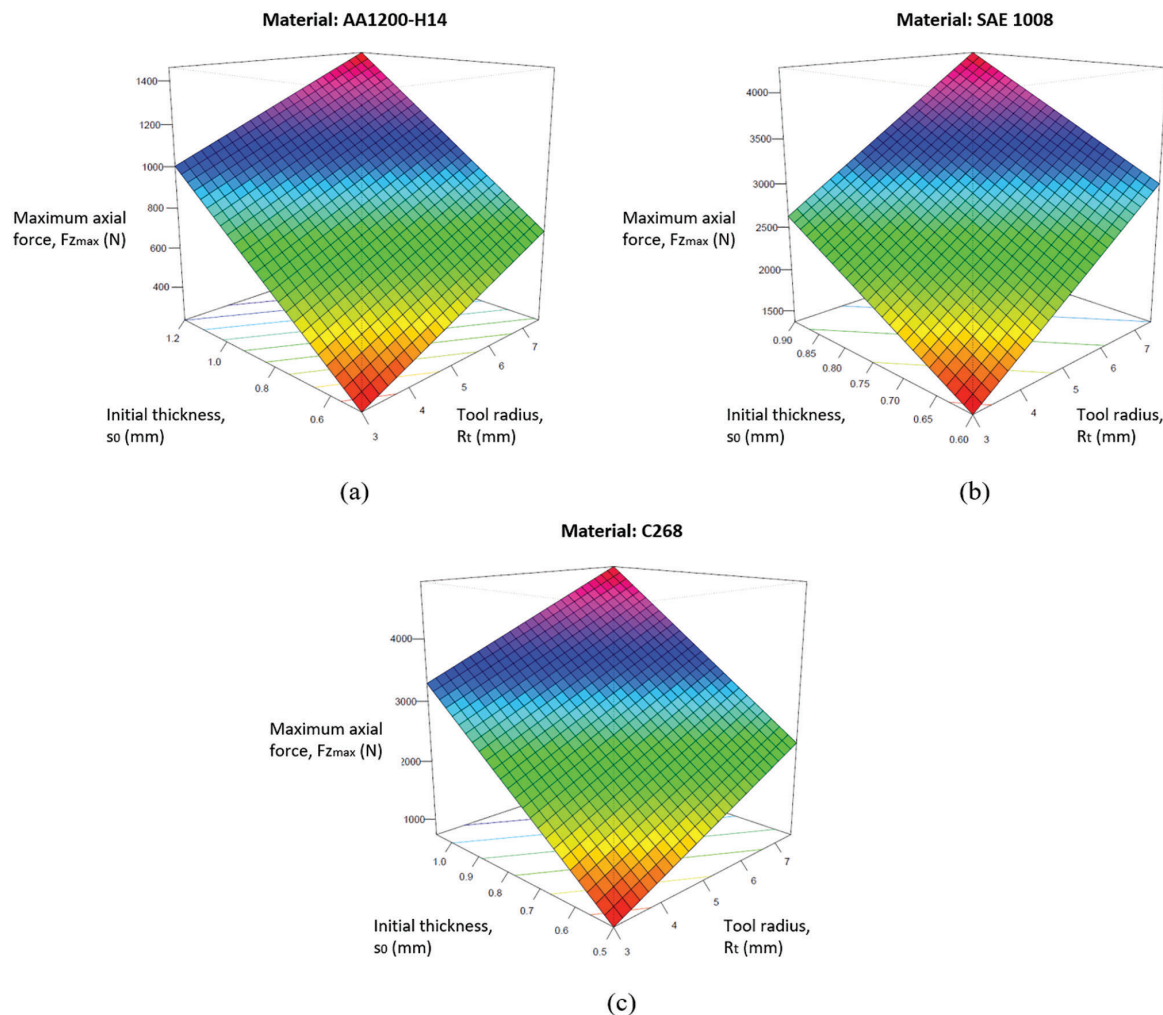


Figure 9: Graph for Fz_{max} response surface according to s_0 and R_t for AA1200-H14 (a), SAE1008 (b) and C268 (c).

varies according to Equation 7, and this variation occurs differently for each material, as they have different mechanical properties.

3.3. FEM results

The axial force versus time graphs obtained in the FEM simulations was compared to the experimental graphs. The percentage errors in the maximum axial force estimate varied between 4.6 and 9.5 %, as indicated in Table 5. This low percentage error margin allows us to conclude that the force data obtained in the FEM simulation were in agreement with the data seen in the experiments.

The MAE and RMSE values calculated for the FEM sub-models were 99.3 and 103.0, respectively. These values are very similar to those obtained by prediction model 3, obtained by the multiple linear regression (Equation 7), in which the MAE and RMSE values were 96.6 and 139.8.

Figure 10 indicates the experimental graph and the FEM simulation for the 25th experiment. This Figure also indicates the point where the beginning of the crack appears (experimental graph), and shows the maximum force point in the previous step-down, which was used as a comparison measure between the two graphs. In Figure 10 it is also possible to identify the same tendency for force elevation in both graphs, even if the peak points are better described by the simulation than the mean force points (inferior level).

As indicated in Figure 10, the force is overestimated by the model of finite elements when compared to the data found in the experiments, mainly at the beginning of the graph. This difference was also verified in the studies by NETO *et al.* [25], which attributed this fact to a possible slide between the sheet and the blank-holder, something that was not considered in the simulation.

As indicated in Figure 11(a), using the FEM simulation results for thickness, it is possible to identify the location of the smallest thickness predicted by the finite element model. This thickness reduction site coincides with the place where the crack was identified in the experiment.

Table 5: FEM results for axial force.

| EXP. | EXPERIMENTAL OUTPUTS | FEM MODEL PREDICTED OUTPUTS | PERCENTAGE ERROR (%) |
|------|----------------------|-----------------------------|----------------------|
| | Fz_{max} (N) | Fz_{max} (N) | |
| 7 | 638.9 | 699.6 | 5.5 |
| 14 | 2668.5 | 2790.0 | 4.6 |
| 25 | 2110.8 | 1995.2 | 9.5 |

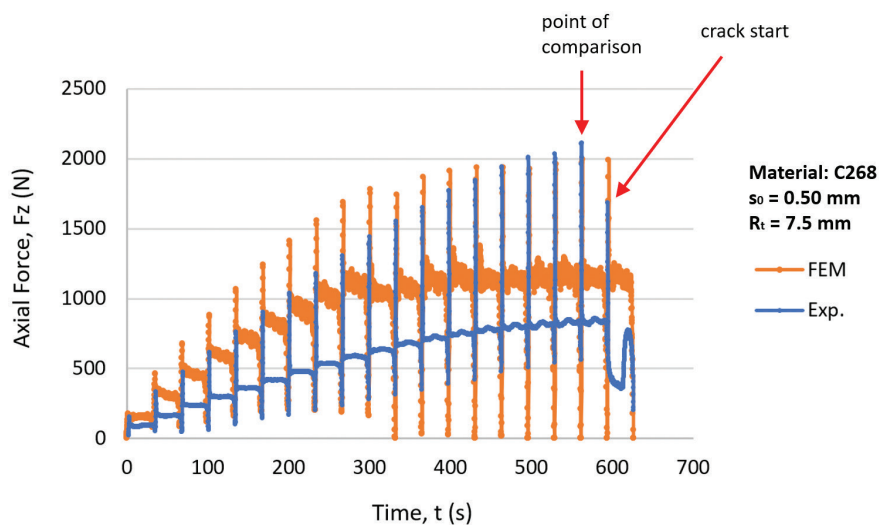


Figure 10: Graph comparing forces between experimental and FEM simulation values for C268 with $s_0 = 0.50$ mm and $R_t = 7.5$ mm.

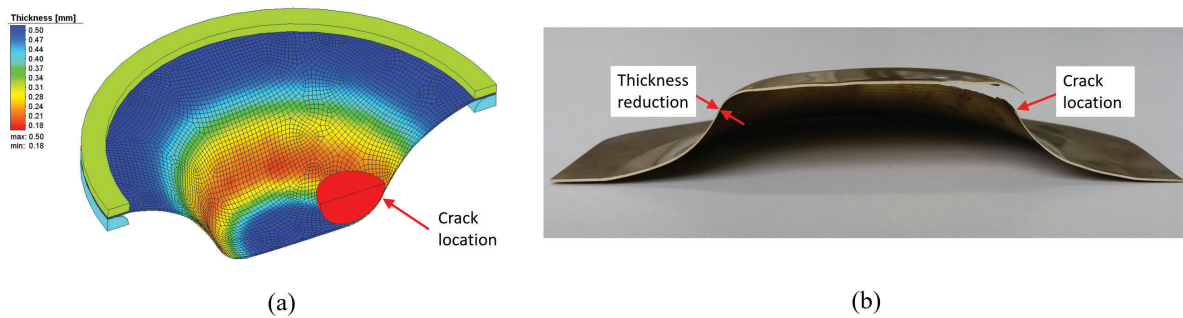


Figure 11: FEM simulation with thickness results (a) and location of the crack in the sheet in the 25th experiment (b).

4. CONCLUSIONS

In this study, we evaluated the influence of the tool radius, the initial thickness, and the sheets' material properties (C and n) on the maximum axial force required for the SPIF process. After concluding the experiments, FEM simulations, and multiple regressions, it is possible to conclude that:

- Maximum axial force could be estimated by linear regression equation, for different materials, according to R_p , s_0 , C , and n , with R^2 of 98.85% and maximum percentage error of 11.5%;
- The increase in tool radius, initial sheet thickness, and strength coefficient, as well as the reduction in the strain-hardening exponent, increases in maximum axial force required for the SPIF process. In addition, the interactions between these parameters also influence the maximum axial force;
- The creation of a linear regression model as a function of the mechanical properties C and n , instead of R_m , showed better accuracy in predicting the maximum axial force, regardless of the material selected;
- The FEM simulation sub-models showed good accuracy to predict the maximum axial forces in SPIF. In these simulations, the maximum percentage error was 9.5%. Furthermore, the MAE and RMSE values were similar to those obtained by the best regression model developed in this work.

5. REFERENCES

- [1] KUMAR, S.P., ELANGO VAN, S., MOHANRAJ, R., *et al.*, "A comprehensive review in incremental forming on approaches of deformation analysis and surface morphologies", *Materials Today: Proceedings*, v. 43, pp. 3129–3139, 2021. doi: <http://dx.doi.org/10.1016/j.matpr.2021.01.599>.
- [2] MORE, K.R., SISODIA, V., KUMAR, S., "A brief review on formability, wall thickness distribution and surface roughness of formed part in incremental sheet forming, advances in manufacturing processes", In: Dave, H.K., Nedelcu, D. (eds), *Advances in manufacturing processes*, Singapore, Springer, pp. 135–149, 2021. doi: http://dx.doi.org/10.1007/978-981-15-9117-4_11.
- [3] SCHEFFLER, S., PIERER, A., SCHOLZ, P., *et al.*, "Incremental sheet metal forming on the example of car exterior skin parts", *Procedia Manufacturing*, v. 29, pp. 105–111, 2019. doi: <http://dx.doi.org/10.1016/j.promfg.2019.02.112>.
- [4] SCHREIBER, R.G., SOUSA, A.L., SANTOS, E.M., *et al.*, "Incremental sheet forming parameters and applications: a review", *Brazilian Journal of Development*, v. 8, n. 8, pp. 58036–58060, 2022. doi: <http://dx.doi.org/10.34117/bjdv8n8-207>.
- [5] CHANG, Z., LI, M., CHEN, J., "Analytical modeling and experimental validation of the forming force in several typical incremental sheet forming processes", *International Journal of Machine Tools & Manufacturing*, v. 140, pp. 62–76, 2019. doi: <http://dx.doi.org/10.1016/j.ijmachtools.2019.03.003>.
- [6] DABWAN, A., RAGAB, A.E., SALEH, M.A., *et al.*, "Study of the effect of process parameters on surface profile accuracy in single-point incremental sheet forming of AA1050-H14 aluminum alloy", *Advances in Materials Science and Engineering*, v. 2020, pp. 7265941, 2020. doi: <http://dx.doi.org/10.1155/2020/7265941>.
- [7] MOHANTY, S., REGALLA, S.P., RAO, Y.V.D., "Effect of inclination and rotation of the sheet on sheet thinning and formability in robot assisted incremental sheet metal forming", *Materials Today: Proceedings*, v. 46, pp. 1039–1049, 2021. doi: <http://dx.doi.org/10.1016/j.matpr.2021.01.228>.

- [8] SCHREIBER, R.G., SCHAEFFER, L., “Manufacture of absorber fins for solar collector using incremental sheet forming”, *Journal of Materials Research and Technology*, v. 8, n. 1, pp. 1132–1140, 2019. doi: <http://dx.doi.org/10.1016/j.jmrt.2018.07.018>.
- [9] AMBROGIO, G., FILICE, L., GAGLIARDI, F., “Improving industrial suitability of incremental sheet forming process”, *International Journal of Advanced Manufacturing Technology*, v. 58, n. 9–12, pp. 941–947, 2012. doi: <http://dx.doi.org/10.1007/s00170-011-3448-6>.
- [10] BEN SAID, L., BOUHAMED, A., WALI, M., *et al.*, “SPIF manufacture of a dome part made of AA1060-H14 aluminum alloy using cnc lathe machine: numerical and experimental investigations”, *Arabian Journal for Science and Engineering*, v. 46, n. 12, pp. 12207–12220, 2021. doi: <http://dx.doi.org/10.1007/s13369-021-05919-7>.
- [11] SCHREIBER, R.G., ARALDI, A., KINIZ JÚNIOR, M., *et al.*, “Failure criterion for SPIF based on mean stress”, *Journal of the Brazilian Society of Mechanical Sciences and Engineering*, v. 44, n. 5, pp. 1–11, 2022. doi: <http://dx.doi.org/10.1007/s40430-022-03508-9>.
- [12] ISMAIL, N.A., ISMAIL, M.I.S., RADZMAN, M.A.M., *et al.*, “Parametric optimization of robot-based single point incremental forming using Taguchi method”, *International Journal of Integrated Engineering*, v. 11, n. 1, pp. 217–224, 2019. doi: <http://dx.doi.org/10.30880/ijie.2019.11.01.023>.
- [13] PRAKASH SINGH, R., KUMAR GUPTA, S., KUMAR SINGH, P., *et al.*, “Robot assisted incremental sheet forming of Al6061 under static pressure: preliminary study of thickness distribution within the deformation region”, *Materials Today: Proceedings*, v. 47, pp. 2737–2741, 2021. doi: <http://dx.doi.org/10.1016/j.matpr.2021.03.056>.
- [14] SCHREIBER, R.G., KINIZ JÚNIOR, M., FIUZA FILHO, F., *et al.*, “Influência dos parâmetros de estampagem incremental na estampabilidade de chapas de alumínio puro”, *Revista Matéria*, v. 27, n. 1, pp. e13140, 2022. doi: <http://dx.doi.org/10.1590/s1517-707620220001.1340>.
- [15] AMINO, M., MIZOGUCHI, M., TERAUCHI, Y., *et al.*, “Current status of “Dieless” Amino’s incremental forming”, *Procedia Engineering*, v. 81, pp. 54–62, 2014. doi: <http://dx.doi.org/10.1016/j.proeng.2014.09.128>.
- [16] AZEVEDO, N.G., FARIAS, J.S., BASTOS, R.P., *et al.*, “Lubrication aspects during Single Point Incremental Forming for steel and aluminum materials”, *International Journal of Precision Engineering and Manufacturing*, v. 16, n. 3, pp. 589–595, 2015. doi: <http://dx.doi.org/10.1007/s12541-015-0079-0>.
- [17] CENTENO, G., BAGUDANCH, I., MARTÍNEZ-DONAIRE, A.J., *et al.*, “Critical analysis of necking and fracture limit strains and forming forces in single-point incremental forming”, *Materials & Design*, v. 63, pp. 20–29, 2014. doi: <http://dx.doi.org/10.1016/j.matdes.2014.05.066>.
- [18] JESWIET, J., MICARI, F., HIRT, G., *et al.*, “Asymmetric single point incremental forming of sheet metal”, *CIRP Annals Manufacturing Technology*, v. 54, n. 2, pp. 88–114, 2005. doi: [http://dx.doi.org/10.1016/S0007-8506\(07\)60021-3](http://dx.doi.org/10.1016/S0007-8506(07)60021-3).
- [19] AERENS, R., EYCKENS, P., VAN BAEL, A., *et al.*, “Force prediction for single point incremental forming deduced from experimental and FEM observations”, *International Journal of Advanced Manufacturing Technology*, v. 46, n. 9–12, pp. 969–982, 2010. doi: <http://dx.doi.org/10.1007/s00170-009-2160-2>.
- [20] TORSAKUL, S., KUPTASTHIEN, N., “Effects of three parameters on forming force of the single point incremental forming process”, *Journal of Mechanical Science and Technology*, v. 33, n. 6, pp. 2817–2823, 2019. doi: <http://dx.doi.org/10.1007/s12206-019-0528-2>.
- [21] AL-OBAIDI, A., KRÄUSEL, V., LANDGREBE, D., “Hot single-point incremental forming assisted by induction heating”, *International Journal of Advanced Manufacturing Technology*, v. 82, n. 5–8, pp. 1163–1171, 2016. doi: <http://dx.doi.org/10.1007/s00170-015-7439-x>.
- [22] PEREIRA BASTOS, R.N., ALVES DE SOUSA, R.J., FERNANDES FERREIRA, J.A., “Enhancing time efficiency on single point incremental forming processes”, *International Journal of Material Forming*, v. 9, n. 5, pp. 653–662, 2016. doi: <http://dx.doi.org/10.1007/s12289-015-1251-x>.
- [23] DUFLOU, J., TUNÇKOL, Y., SZEKERES, A., *et al.*, “Experimental study on force measurements for single point incremental forming”, *Journal of Materials Processing Technology*, v. 189, n. 1–3, pp. 65–72, 2007. doi: <http://dx.doi.org/10.1016/j.jmatprot.2007.01.005>.
- [24] LI, Y., DANIEL, W.J.T., MEEHAN, P.A., “Deformation analysis in single-point incremental forming through finite element simulation”, *International Journal of Advanced Manufacturing Technology*, v. 88, n. 1–4, pp. 255–267, 2017. doi: <http://dx.doi.org/10.1007/s00170-016-8727-9>.

- [25] NETO, D.M., MARTINS, J.M.P., OLIVEIRA, M.C., *et al.*, “Evaluation of strain and stress states in the single point incremental forming process”, *International Journal of Advanced Manufacturing Technology*, v. 85, n. 1–4, pp. 521–534, 2016. doi: <http://dx.doi.org/10.1007/s00170-015-7954-9>.
- [26] WANG, J., NAIR, M., ZHANG, Y., “An efficient force prediction strategy in single point incremental sheet forming”, *Procedia Manufacturing*, v. 5, pp. 761–771, 2016. doi: <http://dx.doi.org/10.1016/j.promfg.2016.08.062>.
- [27] DUFLOU, J.R., TUNCKOL, Y., AERENS, R., “Force analysis for single point incremental forming”, *Key Engineering Materials*, v. 344, pp. 543–550, 2007. doi: <http://dx.doi.org/10.4028/www.scientific.net/KEM.344.543>.
- [28] LI, Y.L., LIU, Z.B., LU, H.B., *et al.*, “Experimental study and efficient prediction on forming forces in incremental sheet forming”, *Advanced Materials Research*, v. 939, pp. 313–321, 2014. doi: <http://dx.doi.org/10.4028/www.scientific.net/AMR.939.313>.
- [29] BANSAL, A., LINGAM, R., YADAV, S.K., *et al.*, “Prediction of forming forces in single point incremental forming”, *Journal of Manufacturing Processes*, v. 28, pp. 486–493, 2017. doi: <http://dx.doi.org/10.1016/j.jmapro.2017.04.016>.
- [30] LOSTADO, R., MARTINEZ, R.F., MAC DONALD, B.J., “Determination of the contact stresses in double-row tapered roller bearings using the finite element method, experimental analysis and analytical models”, *Journal of Mechanical Science and Technology*, v. 29, n. 11, pp. 4645–4656, 2015. doi: <http://dx.doi.org/10.1007/s12206-015-1010-4>.
- [31] FERNANDEZ MARTINEZ, R., LOSTADO LORZA, R., SANTOS DELGADO, A.A., *et al.*, “Optimizing presetting attributes by softcomputing techniques to improve tapered roller bearings working conditions”, *Advances in Engineering Software*, v. 123, pp. 13–24, 2018. doi: <http://dx.doi.org/10.1016/j.advengsoft.2018.05.005>.
- [32] LORZA, R.L., BOBADILLA, M.C., CALVO, M.Á.M., *et al.*, “Residual stresses with time-independent cyclic plasticity in finite element analysis of welded joints”, *Metals*, v. 7, n. 4, pp. 136, 2017.
- [33] LOSTADO LORZA, R., ESCRIBANO GARCÍA, R., FERNANDEZ MARTINEZ, R., *et al.*, “Using genetic algorithms with multi-objective optimization to adjust finite element models of welded joints”, *Metals*, v. 8, n. 4, pp. 230, 2018. doi: <http://dx.doi.org/10.3390/met8040230>.
- [34] ILLERA, M., LOSTADO, R., FERNANDEZ MARTINEZ, R.F., *et al.*, “Characterization of electrolytic tinplate materials via combined finite element and regression models”, *Journal of Strain Analysis for Engineering Design*, v. 49, n. 6, pp. 467–480, 2014. doi: <http://dx.doi.org/10.1177/0309324714524398>.
- [35] ÍÑIGUEZ-MACEDO, S., LOSTADO-LORZA, R., ESCRIBANO-GARCÍA, R., *et al.*, “Finite element model updating combined with multi-response optimization for hyper-elastic materials characterization”, *Materials (Basel)*, v. 12, n. 7, pp. 1019, 2019. doi: <http://dx.doi.org/10.3390/ma12071019>. PubMed PMID: 30934792.
- [36] ESCRIBANO, R., LOSTADO, R., MARTÍNEZ-DE-PISÓN, F.J., *et al.*, “Modelling a skin-pass rolling process by means of data mining techniques and finite element method”, *Journal of Iron and Steel Research International*, v. 19, n. 5, pp. 43–49, 2012. doi: [http://dx.doi.org/10.1016/S1006-706X\(12\)60098-3](http://dx.doi.org/10.1016/S1006-706X(12)60098-3).
- [37] SCHREIBER, R.G., TEIXEIRA, A.R., PEREIRA, R.S.F., *et al.*, “Prototyping of absorber plate for solar collector by ISF and FSW processes”, *Journal of the Brazilian Society of Mechanical Sciences and Engineering*, v. 43, n. 7, pp. 1–12, 2021. doi: <http://dx.doi.org/10.1007/s40430-021-03083-5>.
- [38] HAAG, J., FERRANTI, G.O. “Estampabilidade de aços de baixo carbono”, In: *54 Seminário de Laminação e Conformação*, pp. 308–319, 2017. doi: <http://dx.doi.org/10.5151/1983-4764-30515>.
- [39] MAXIMILIANO, G., SCHAEFFER, L., DALEFFE, A., *et al.* “Estampagem incremental de múltiplos passes em chapa de latão C268”, In: *36º SENAFOR, 19ª Conferência Nacional de Conformação de Chapas, 6ª Conferência Internacional de Conformação de Chapas, 3º Congresso do BrDDR*, 2016.
- [40] KUMAR, A., GULATI, V., KUMAR, P., *et al.*, “Forming force in incremental sheet forming: a comparative analysis of the state of the art”, *Journal of the Brazilian Society of Mechanical Sciences and Engineering*, v. 41, n. 6, pp. 1–45, 2019. doi: <http://dx.doi.org/10.1007/s40430-019-1755-2>.